Supplementary Information (SI) for Journal of Materials Chemistry C.
This journal is © The Royal Society of Chemistry 2026

Ge-Doping-Induced Phase Engineering of *β*/*ε*-Ga_2O_3 for High-Performance Ultraviolet Detector

Jiahui Xie[1], Chen Li[2], Xinyu Liu[1], Guodong Wang[*,1], Yyuan Liu[1], Han Yan[1], Yang Li[1], Xiaohu Hou[2], Tao Qi[*,4], Wenxiang Mu[*,1,3]

[1] State Key Laboratory of Crystal Materials, Institute of Novel Semiconductors, Institute of Crystal Materials, Shandong University, Jinan, Shandong, 250100, China

[2] School of Microelectronics University of Science and Technology of China Hefei 230026, China

[3] Shenzhen Research Institute of Shandong University, Virtual University Park in South District, Shenzhen 518057, China

[4] Jinan Jingheng Electronics Co.,Ltd, No. 13856, West Jingshi Road,Ping'an Subdistrict, Changqing District, Jinan City, Shandong Province, P.R.China.

* Corresponding author.

E-mail addresses: guodong9631@sdu.edu.cn (Guodong Wang), jinanqt@126.com (Tao Qi), mwx@sdu.edu.cn (Wenxiang Mu).

Gallium oxide (Ga_2O_3) thin films with varying Germanium (Ge) doping concentrations were heteroepitaxially grown on sapphire substrates using Mist-CVD (detailed parameters are provided in the Experimental Section). The growth was conducted under a mixed Ar/O_2 atmosphere. Precursor solutions were prepared with nominal Ge/Ga molar ratios of 0% (Sample F1), 0.1% (Sample F2), 0.5% (Sample F3), and 1% (Sample F4). As illustrated in Fig. S1(a), the incorporation of Ge induces a distinct shift in the X-ray diffraction (XRD) peaks. specifically, the diffraction peaks for samples F2–F4 shift toward higher angles relative to the undoped sample F1. Notably, this shift stabilizes for samples F3 and F4. Multi-point XRD scanning of Sample F2 (the primary Ge-doped sample discussed in the main text) reveals a mixed-phase structure comprising both *β*- and ε-Ga_2O_3, as shown in Fig. S1(b).

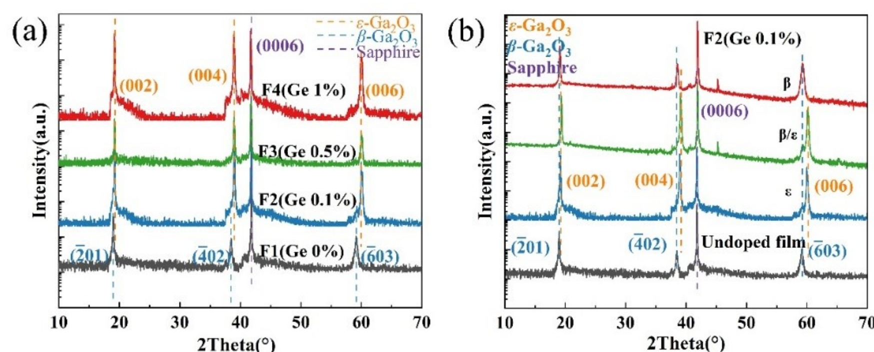

Figure S1 XRD 2θ curves of Ga_2O_3 thin film samples grown on sapphire substrates:

(a) F1~F4 samples(b) F1 and F2 sample

To further elucidate the phase composition and crystalline quality, high-resolution XRD omega and phi scans were performed. The results confirm that the undoped sample F1 consists of pure β-Ga_2O_3, while sample F2 (0.1% Ge) exhibits a β/ε mixed-phase structure. Samples F3 (0.5% Ge) and F4 (1% Ge) are identified as pure ε-Ga_2O_3. Interestingly, the crystalline quality of the films improves with increasing Ge concentration, likely due to the relaxation of lattice strain[1] afforded by Ge incorporation. The full width at half maximum (FWHM) reaches a minimum of 0.55° for the ε-Ga_2O_3 film with 0.5% Ge doping. Although the FWHM slightly degrades to 0.62° at 1% Ge doping, the ε-phase remains stable. These findings suggest that Ge doping effectively stabilizes the ε-phase, thereby expanding the growth window for this metastable polymorph at elevated temperatures.

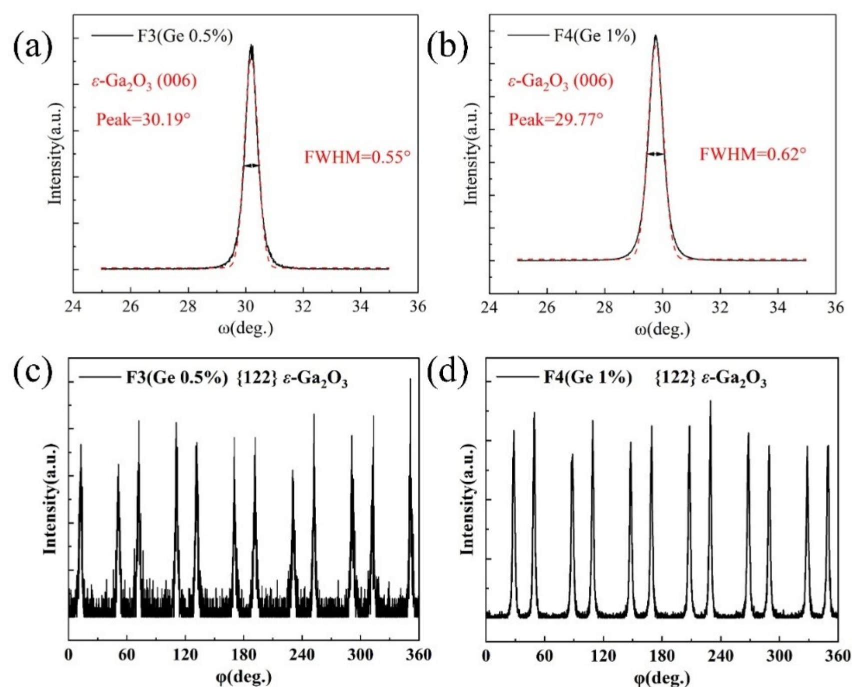

Figure S2 High-resolution XRD omega scans: (a) F3 ε-Ga_2O_3 (006) crystal plane (b) F4 ε-Ga_2O_3 (006) crystal plane High-resolution XRD phi scans: (c) F3 ε-Ga_2O_3 (006) plane (d) F4 ε-Ga_2O_3 (006) plane

Figure 3 and Figure 4 present the cross-sectional SEM images and surface AFM morphologies of the films. The Ga_2O_3 film thickness is approximately 500–600 nm. After Ge doping, hillock-like protrusions appear on the film surface, which may be attribute to the effective incorporation of Ge and the formation of a mixed phase at the microscopic level.

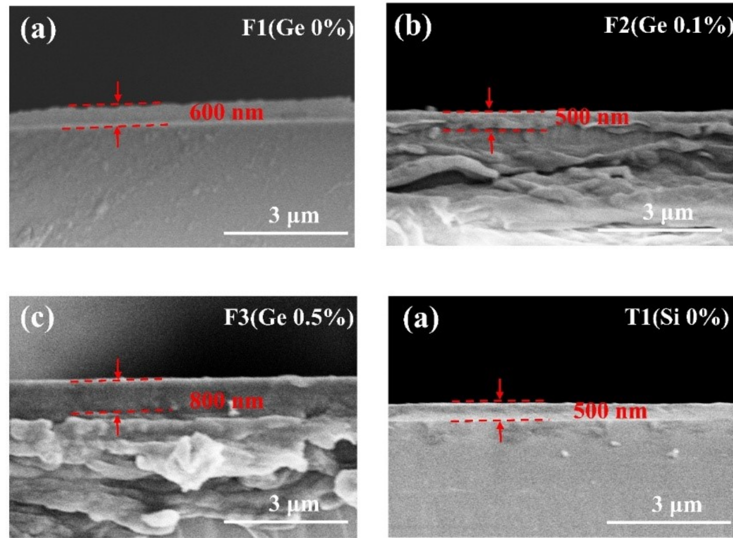

Figure S3 SEM cross-sectional images of Ga_2O_3 films: (a) undoped sample (b) 0.1% Ge doped sample (c) 0.5% Ge doped sample (d) 1% Ge doped sample

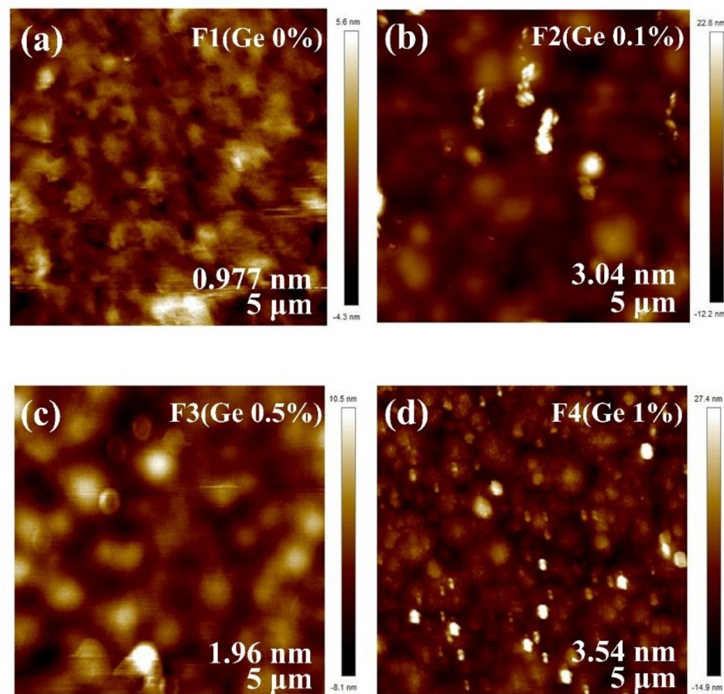

Figure S4 AFM surface topography images: (a) undoped sample (b) 0.1% Ge doped sample (c) 0.5% Ge doped sample (d) 1% Ge doped sample

To further analyze the distribution of the β/ε-Ga_2O_3 mixed phase in the F2 sample, the phase structure was examined using EBSD. The Kikuchi diffraction patterns from the EBSD were calibrated to determine that the crystal orientations of the substrate were the (001) and (-201) planes (Fig. S5(a)), corresponding to ε-Ga_2O_3 and β-Ga_2O_3, respectively. The EBSD BC scan (Fig. S5(b)) reveals numerous grain-

like structures distributed across the smooth epitaxial film surface. The phase scan results (Fig. S5(c)) clearly distinguish the phase distributions of β-Ga_2O_3 (blue) and ε-Ga_2O_3 (red). On the β-Ga_2O_3 matrix, Ge doping induces the formation and growth of ε-Ga_2O_3 grains in certain regions, resulting in a non-uniform, patchy distribution.

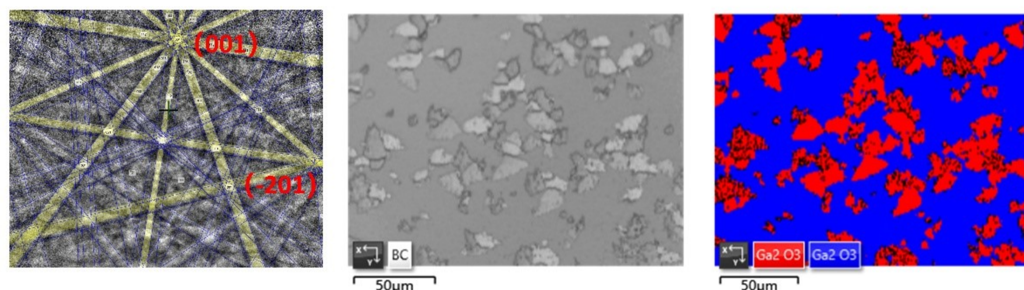

Figure S5 EBSD analysis of the F2 mixture sample (0.1% Ge β/ε-Ga2O3) (a) EBSD pattern (b) EBSD BC scan (c) EBSD phase distribution map

X-ray photoelectron spectroscopy (XPS) was employed to investigate the chemical states and defect characteristics of the films. Binding energies were calibrated using the C 1s peak at 284.8 eV. The survey spectra (Fig. S6(a)) exhibit additional Ge-related signals in the doped samples. High-resolution spectra for the O 1s and Ga 3p core levels are presented in Figs. S6(b) and (c), respectively. Minor peak shifts are observed, attributed to the surface-sensitive nature of XPS and the influence of film defects. Gaussian fitting of the Ge 3d core level for samples F2–F4 (Fig. S6(d)) reveals a monotonic increase in peak intensity around 32.2 eV with increasing doping concentration. For Sample F2 (0.1% Ge), the calculated atomic percentages for Ga 3d and Ge 3d are 92.27% and 1.6%, respectively, yielding a Ge/Ga ratio of 0.017. Similarly, Sample F3 shows a Ge/Ga ratio of 0.033 (Ga/O = 0.99), and Sample F4 shows a Ge/Ga ratio of 0.098 (Ga/O = 0.87), as summarized in Fig. S6(e). The deviation of the Ga/O ratio from ideal stoichiometry with increasing Ge content may stem from two factors: (i) the competitive occupation of tetrahedral and octahedral sites by Ge and Ga, and (ii) the generation of defects such as oxygen vacancies at high doping levels, although moderate doping (e.g., 0.1%) appears to compensate for intrinsic defects[2]. Valence band (VB) spectra (Fig. S6(f)) show that the valence band maximum (VBM) shifts from 2.84 eV to 2.61 eV as Ge doping increases from 0% to 0.1%, consistent with the β-to-ε phase transition. Further doping to 1% (pure ε-phase) results in a VBM shift to higher binding energies (3.00 eV for F3, 3.20 eV for F4).

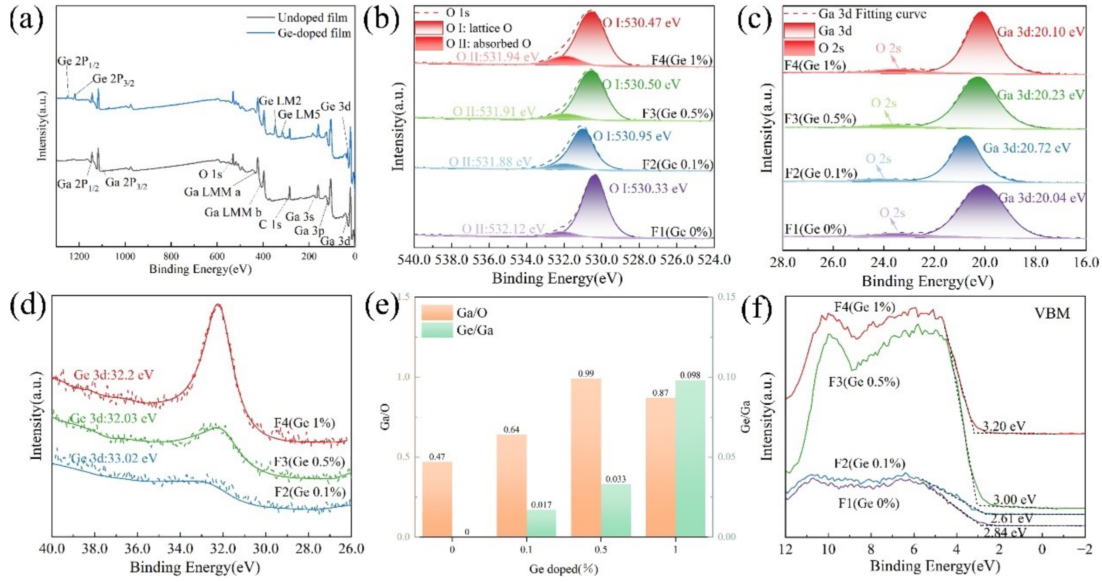

Figure S6 XPS spectra: (a) Full scan from 0 to 1200 eV (b) O 1s core level (c) Ga 3d core level (d) Ge 3d core level (e) Relationship between Ga/O and Ge/O ratios versus Ge doping concentration (f) Valence band spectra

Excitation tests were conducted on the F1 and F2 samples using PL spectroscopy. Figure S7 shows that, following the incorporation of 0.1% Ge, the V_{Ga} defects in the film were quenched, which is attributed to the optimization of the crystal structure and chemical composition. The introduction of Ge not only acts as a compatible atom that can occupy positions in the Ga tetrahedra and octahedra to stabilize the lattice structure, thereby improving lattice integrity, but also functions as a surface activator to optimize growth kinetics. This effectively suppresses the formation of V_{Ga}, restoring the stoichiometric ratio to a value close to the ideal, and laying a solid material foundation for subsequent photogenerated carrier transport.

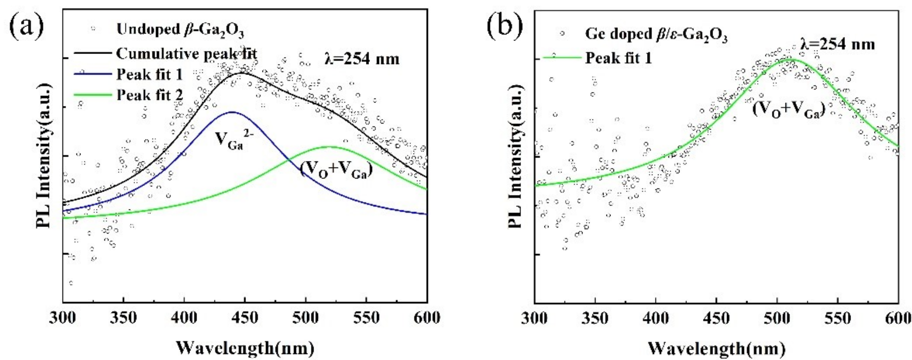

Figure S7 PL spectra of (a) undoped and (b) Ge-doped samples

To interpret the VBM shifts, optical bandgaps (E_g) were extracted from UV-Vis transmission spectra (Fig. S8(a)). As shown in Fig. S8(b), the extracted bandgaps for samples F1–F4 are 5.15 eV, 4.90 eV, 5.22 eV, and 5.24 eV, respectively. The F3 and F4 samples have transformed into the pure ε phase; the intrinsic differences in this

crystal phase contribute the fundamental blue-shift component to the increase in its optical bandgap. Furthermore, as the Ge doping concentration increases, lattice distortion occurs in ε-Ga_2O_3, and the Burstein-Moss effect causes the bandgap width to increase to 5.24 eV[3]. To further analyze the bandgap variation of the F2 mixed-phase sample (Ge 0.1% β/ε-Ga_2O_3), multi-point measurements were performed on this sample. Figures S8(c) and (d) reveal two distinguishable bandgap regions. Corresponding to the results of the XRD multi-point measurements, the β-Ga_2O_3 region in the mixed-phase film corresponds to an E_g of 4.9–5.0 eV, while the ε-Ga_2O_3 region corresponds to an E_g of approximately 5.2 eV.

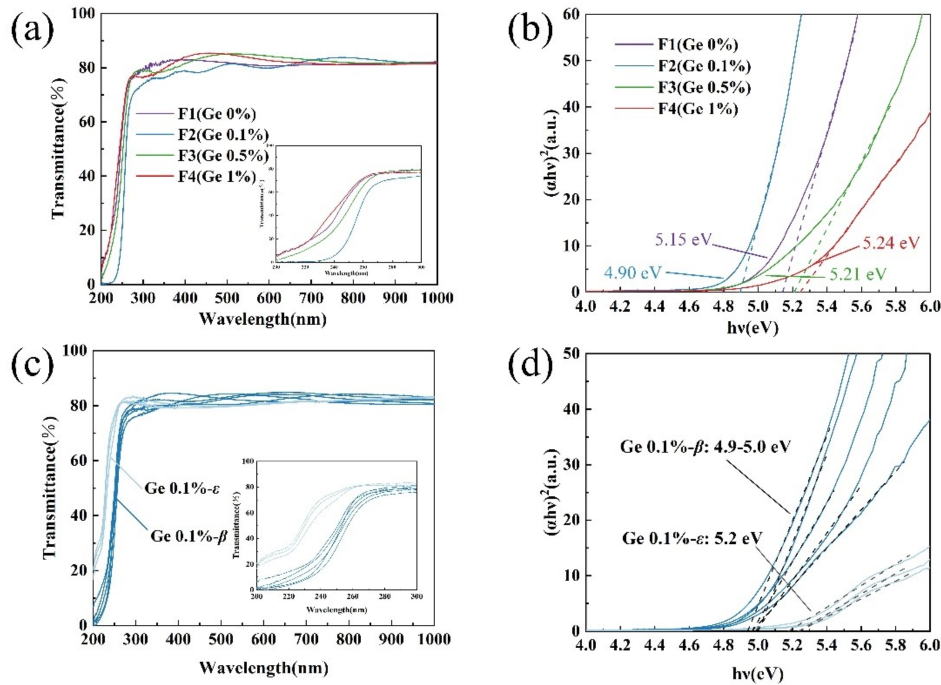

Figure S8 (a) Transmission spectra of F1-F4 Ga_2O_3 films (b) $(ah\nu)^2$ vs hν plot (c) Transmission spectra of F2 Ga_2O_3 films (d) $(ah\nu)^2$ vs hν plot

The introduction of 0.1% Ge doping has favorably influenced the structural properties of the β-Ga_2O_3 thin film material. Furthermore, the appropriate amount of Ge shallow donor energy levels has enhanced the carrier concentration within the film, laying an excellent material foundation for phase engineering. As shown in Figure S9, the carrier transport mechanism within the material has been fully optimized. In undoped β-Ga_2O_3 films, lattice mismatch during the heteroepitaxial growth process results in the presence of deep-level defects (V_{Ga}) within the material, which act as effective “trapping centers” or “non-radiative recombination centers” during carrier transport. When photons excite electrons to transition from the valence band to the conduction band, the photo-generated electrons are easily captured by these deep-level traps, resulting in shortened carrier lifetime and an inability to participate in effective long-range transport. This manifests as a low photocurrent response and poor detection efficiency. In contrast, Ge, as a shallow-donor impurity, introduces Ge donor levels when doped beneath the CBM. This modification yields a threefold optimization effect: 1. Shallow-donor ionization: Electrons at the Ge donor energy

level can transition to the conduction band via thermal or photoexcitation, appropriately increasing the background carrier concentration and filling some of the deep-level traps, thereby reducing the probability of photo-generated carriers being recaptured. 2. Defect Suppression: The introduction of Ge atoms effectively optimizes the film's lattice structure and chemical composition, suppressing the formation of V_{Ga} and reducing the electron capture pathways shown in Figure S9(a). Photogenerated electrons can transition more smoothly and directly to the conduction band and remain in a free state, significantly extending the carrier lifetime. 3. β/ε Type-II Band Alignment: With the introduction of doping, Ge-induced epitaxial films form stable ε-Ga_2O_3 regions in certain areas, creating a natural Type-II band alignment at the surface. For example, using the intrinsic VBM values of the F1 and F3 samples to represent the β-Ga_2O_3 and ε-Ga_2O_3 regions, respectively, at the interface between the two phases in the F2 mixed-phase sample, the Fermi levels align, forming a barrier with ΔE_C=0.89 eV and ΔE_V=0.59 eV, which facilitates the separation and collection of photo-generated electrons.

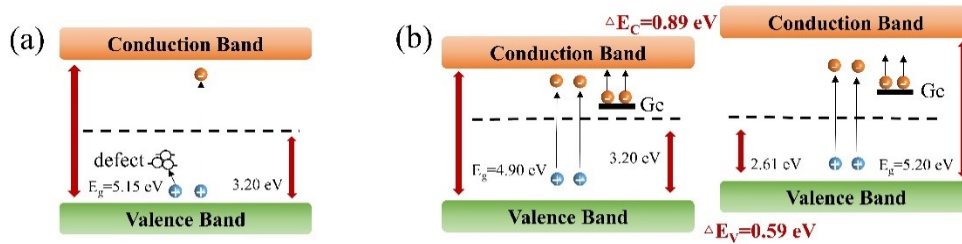

Figure S9 Suppression of deep level defects and band structure tuning within the material upon Ge doping

Lateral metal-semiconductor-metal (MSM) photodetectors were fabricated based on samples F1–F4 (schematic in Fig. S10(a)). Under 254 nm UV illumination, photogenerated carriers are collected by the electrodes, producing a measurable photocurrent. The I-V characteristics (±10 V) are shown in Figs. S10(b) and (c). Samples F3 and F4 exhibit quasi-ohmic behavior with high currents due to their high conductivity, whereas samples F1 and F2 display significantly lower currents, reflecting their higher resistivity. Notably, the dark current density increases dramatically with doping concentration: 10^{-3} $\mu A\cdot cm^{-2}$ for F1, increasing to 10^5 $\mu A\cdot cm^{-2}$ for F4. Maintaining a low dark current is crucial for high-performance photodetection, as it minimizes the noise floor and enhances the detection limit for weak signals. Excessive doping not only degrades crystallinity but also increases leakage current and reduces carrier mobility via impurity scattering[4]. Therefore, this study focuses on the optimized F2 sample (0.1% Ge), using the undoped F1 sample as a reference.

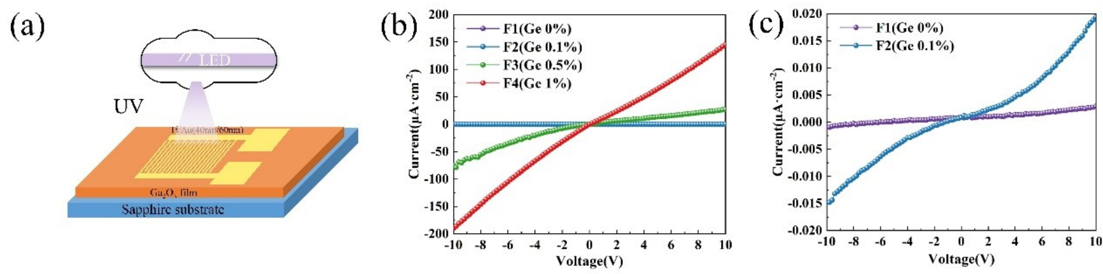

Figure S10 (a) Structural diagram of MSM-type ultraviolet photodetector (b) I-V curves of samples F1–F4 at -10 V to 10 V (c) I-V curves of samples F1 and F2 at -10 V to 10 V

Ga_2O_3 is an intrinsic n-type material. Due to the difference in Fermi levels[5] between the ε phase (N1) and the β phase (N2), spontaneous diffusion of electrons from the higher energy level (N1) to the lower energy level (N2) occurs at the interface, resulting in band bending and the formation of a strong built-in electric field pointing from N1 to N2. The resulting type-II interlaced band structure plays a key role in the photovoltaic effect at zero bias: when ultraviolet light excitation generates electron-hole pairs, the built-in electric field acts as a driving force to rapidly sweep the photo-generated holes into the N2 valence band while pushing the photo-generated electrons toward the N1 conduction band. This spatially oriented separation of photo-generated carriers not only effectively suppresses recombination and extends carrier lifetime, but also establishes a photo-generated electromotive force across the device, thereby realizing self-powered photodetection without the need for an external bias. As shown in Figure S11, when the F2 sample was irradiated with 500 μW/cm² of UV light at 0 V, a photocurrent was detected under the self-powered effect, proving that we have successfully constructed a β/ε II-type heterojunction.

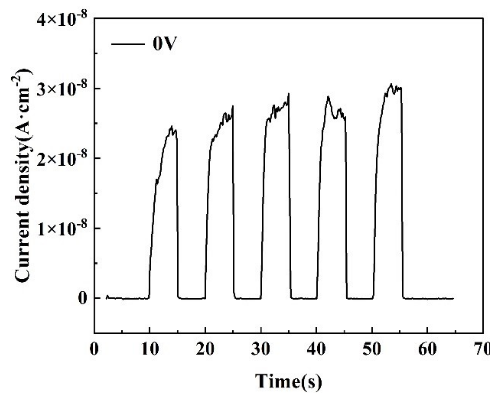

Figure S11 Self-powered response of the F2 (Ge 0.1%) sample at 0 V

Table S1 summarizes the key performance parameters of the F2 sample (0.1% Ge) under 254 nm illumination at a bias of 40 V, as a function of incident optical power density.

Table S1 Ultraviolet Detection Performance of F2 Ga_2O_3 Samples (@40V)

Sample	Power	Responsivity	PDCR	Detectivity	EQE(%)

	denisity ($\mu W/cm^2$)	(A/W)	(I_{photo}/I_{dark})	(Jones)	
	1	10.19	30.5	3.06×10^{13}	4.98×10^{3}
F2(Ge 0.1%)	10	32.54	943	9.78×10^{13}	1.59×10^{4}
	100	100	2.9×10^{4}	3.01×10^{14}	4.88×10^{4}
	500	160	2.32×10^{5}	4.81×10^{14}	7.81×10^{4}

Reference

1. R. J. Zhang, M. Li, G. Wu, L. J. Li, Z. F. Zhang, K. Liang and W. Shen, *Results In Physics*, 2023, **52**, 106916.
2. T. K. O. Vu, D. U. Lee and E. K. Kim, *Journal of Alloys and Compounds*, 2019, **806**, 874-880.
3. J. Y. Zhang, J. Willis, Z. N. Yang, X. Lian, W. Chen, L. S. Wang, X. Y. Xu, T. L. Lee, L. Chen, D. O. Scanlon and K. H. L. Zhang, *CELL REPORTS PHYSICAL SCIENCE*, 2022, **3**.
4. A. K. Singh, C. C. Yen, C. Y. Huang, F. G. Tarntair, H. Y. Chou, S. M. Huang, B. K. Yadlapalli, R. H. Horng and D. S. Wuu, *Mat Sci Semicon Proc.*, 2024, **178**.
5. Y. Lu, P. A. M. Cortez, X. Tang, Z. Y. Liu, V. Khandelwal, S. Krishna and X. H. Li, *Advanced Materials*, 2025, **37**.